Angular dependence of light trapping in $In_{0.3}Ga_{0.7}As/GaAs$ quantum-well solar cells

X. H. Li,[1] P. C. Li,[1] D. Z. Hu,[2] D. M. Schaadt,[2] and E. T. Yu[1]
[1]*Microelectronics Research Center, University of Texas at Austin, 10100 Burnet Rd., Austin, Texas 78758, USA*
[2]*Clausthal Technical University, Institute of Energy Research and Physical Technologies, Clausthal, Germany*

(Received 15 November 2013; accepted 9 January 2014; published online 22 January 2014)

The dependence of light trapping effects in $In_{0.3}Ga_{0.7}As/GaAs$ quantum-well solar cells on wavelength and incident angle is experimentally characterized and analyzed. Separation of active device layers from their epitaxial growth substrate enables integration of thin-film semiconductor device layers with nanostructured metal/dielectric rear contacts to increase optical absorption via coupling to both Fabry-Perot resonances and guided lateral propagation modes in the semiconductor. The roles of Fabry-Perot resonances and coupling to guided modes are analyzed via photocurrent response measurements and numerical modeling for light incident at angles of 0° (normal incidence) to 30° off normal. Light trapping enables external quantum efficiency at long wavelengths as high as 2.9% per quantum well to be achieved experimentally, substantially exceeding the ~1% per quantum well level typically observed. Increased long wavelength quantum efficiency is shown in experimental measurements to persist with increasing angle of incidence and is explained as a consequence of the large number of guided modes available in the device structure. [http://dx.doi.org/10.1063/1.4862931]

I. INTRODUCTION

Light trapping in thin-film solar cells via engineered surface morphology or device geometry, scattering by subwavelength-scale photonic structures, and plasmonic effects has emerged as a promising and highly effective approach for improving optical absorption efficiency, and hence short-circuit current as well as open-circuit voltage via photon recycling effects.[1–5] For typical semiconductor pn junction solar cells, increased optical absorption at long wavelengths is of particular interest as semiconductor absorption coefficients decrease with increasing wavelength. Quantum-well solar cells,[6] in which long-wavelength quantum-well absorption can enable increased photocurrent and power conversion efficiency compared to a conventional pn homojunction solar cell,[7,8] are particularly amenable to performance improvement via light trapping as the optical absorption efficiency in the quantum-well regions is generally low and can be increased to only a limited degree by increasing the number of quantum wells incorporated within the device structure.[9,10]

In this paper, we describe and demonstrate thin-film quantum-well solar cells that are grown by molecular beam epitaxy (MBE), separated from their epitaxial growth substrate, and integrated with large-area, subwavelength-scale metal and dielectric scattering structures on the rear side of the device for long-wavelength light trapping. Such devices exhibit optical absorption efficiency per quantum well substantially higher and at substantially longer wavelengths than in typical quantum-well solar cells that do not exploit light trapping. Furthermore, we present experimental measurements of photocurrent response as a function of the angle at which illumination is incident, and demonstrate that increased absorption due to light trapping persists to angles of incidence at least as large as 30°. Numerical simulations provide detailed insight into the contributions of Fabry-Perot resonances and of scattering into guided optical modes to increased long-wavelength optical absorption as a function of wavelength and incident angle.

II. EXPERIMENT

Sample structures were grown by solid-source MBE on GaAs (001) n-type substrates and are shown schematically in Figure 1(a). For each sample, a 105 nm n-type GaAs buffer layer doped with $\sim 2.5 \times 10^{18}\,cm^{-3}$ Si was grown, followed by a 300 nm n-type ($n \sim 2.5 \times 10^{18}\,cm^{-3}$) $Al_{0.85}Ga_{0.15}As$ sacrificial etch stop layer and 200 nm n-type ($n \sim 2.0 \times 10^{18}\,cm^{-3}$) GaAs. An unintentionally doped layer was then grown consisting of either 84 nm GaAs (for the GaAs pn homojunction structures) or three 4 nm $In_{0.30}Ga_{0.70}As$ quantum wells separated by 17 nm GaAs barriers with 21 nm undoped GaAs layers immediately above and below the quantum-well region (for the quantum-well solar cells). A 1500 nm p-type (Be-doped, $p \sim 5 \times 10^{18}\,cm^{-3}$) GaAs layer and a 20 nm p^+ ($p \sim 5 \times 10^{19}\,cm^{-3}$) GaAs contact layer then completed each epitaxial layer structure. The multiple quantum well structure was designed so that the quantum wells would remain below the critical thickness for strain relaxation.[23] The growth temperature was kept above 500 °C throughout.

Key device fabrication processes are illustrated in Figures 2(a) and 2(b). For devices with a planar metallic back contact, as illustrated in Figure 2(a), 10 nm Cr/40 nm Au/1200 nm In metallization was deposited on the p^+ GaAs surface, then bonded to a Si (001) wafer on which 10 nm Cr/800 nm Au had been deposited by pressing the metalized surfaces together at 180 °C for 20 min. After bonding, the

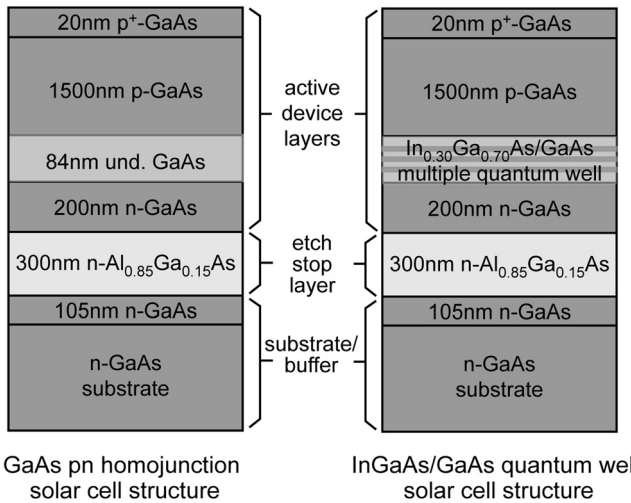

FIG. 1. Schematic diagrams of epitaxial layer structures for (left) GaAs pn homojunction solar cell structure and (right) $In_{0.30}Ga_{0.70}As/GaAs$ quantum-well solar cell structure. Active device layers, etch stop layers, and substrate/buffer layers labeled for each correspond to similarly labeled sample layers in Figure 2.

GaAs substrate was removed by chemical etching in $NH_4OH:H_2O_2$ (1:19) followed by 50% citric acid:H_2O_2 (4:1).[11] The edges of the epitaxial wafer were covered with black wax to prevent etching of the active device layers. The $Al_{0.85}Ga_{0.15}As$ sacrificial etch stop layer was then removed by etching in dilute hydrofluoric acid. 1 mm × 1 mm and 2 mm × 2 mm device mesas were fabricated by photolithography and wet etching, and deposition of AuGe/Ni/Au n-type Ohmic contact metallization completed the device fabrication process.

For devices with nanostructured back contacts for light scattering and trapping, initial metallization of the epitaxially grown p^+-GaAs surface was preceded by e-beam evaporation of 80 nm SiO_2 followed by patterning using nanosphere lithography.[12] In the nanosphere lithography process, illustrated schematically in Figure 2(b), 500 nm diameter polystyrene spheres were deposited on the SiO_2 surface in a hexagonal array using a Langmuir-Blodgett process.[13] An oxygen plasma etch was used to reduce the sphere diameter to 250 nm, followed by deposition of 15 nm Cr, a liftoff

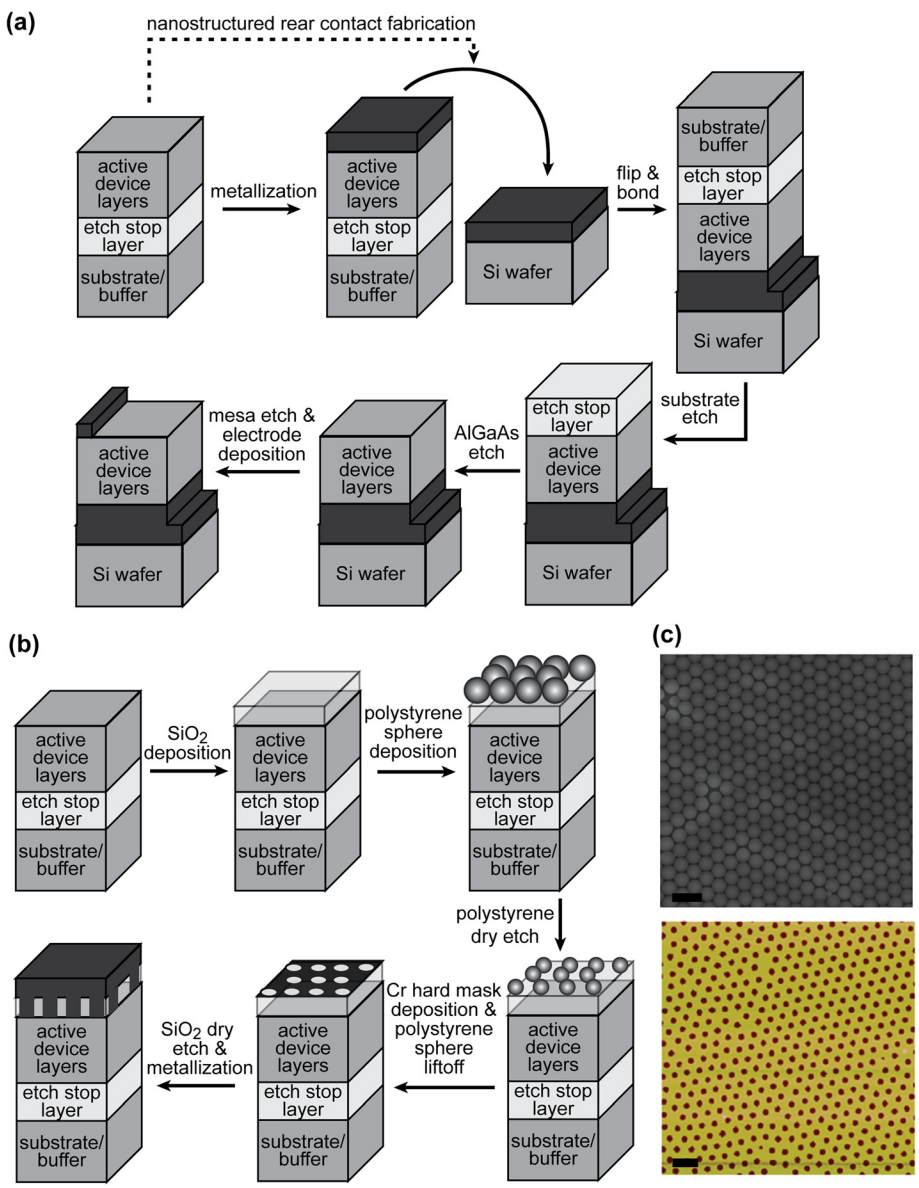

FIG. 2. (a) Key steps in process flow for fabrication of solar cell devices with a planar metallic rear contact. (b) Key steps in process flow for fabrication of nanostructured metal/dielectric rear contacts using nanosphere lithography for patterning. These steps are incorporated into the complete device fabrication process as indicated by the dashed line in (a). (c) Scanning electron micrograph of 500 nm diameter polystyrene spheres deposited by Langmuir-Blodgett process for nanosphere lithography (top), and atomic force microscope topograph of etched hole array in SiO_2 just prior to deposition of contact metallization (bottom). Scale bar for both images is 1 μm.

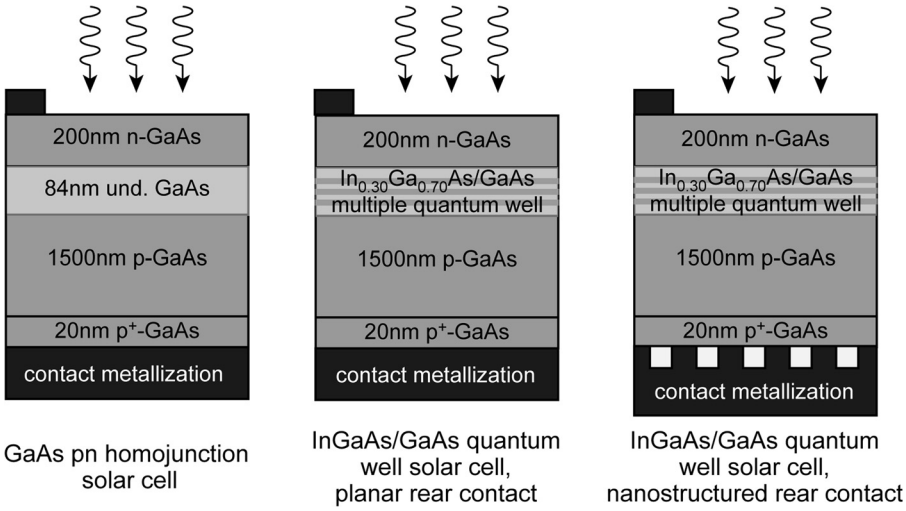

FIG. 3. Schematic diagrams of GaAs pn homojunction reference solar cell structure, InGaAs/GaAs quantum-well solar cell with planar metallic rear contact, and InGaAs/GaAs quantum-well solar cell with nanostructured metal/dielectric rear contact.

process in which the polystyrene spheres were dissolved in toluene, and reactive ion etching of the SiO_2 with a CF_4/O_2 gas mixture. 10 nm Cr/40 nm Au/1200 nm In metallization was then deposited to form the nanostructured back contact; the remainder of the device fabrication process was then the same as that for devices with planar metal back contacts. Figure 2(c) shows a scanning electron micrograph of polystyrene spheres deposited by the Langmuir-Blodgett process, and an atomic force microscope topograph of an etched array of holes in SiO_2 prior to metallization for a nanostructured rear contact. Schematic diagrams of the resulting three types of completed device structures are shown in Figure 3.

Current-voltage characteristics were measured using normally incident light from a Newport Oriel 96000 solar simulator operating at 150 W with an airmass (AM) 1.5G filter. Photocurrent response spectra were measured at zero bias using a single grating monochromator based system from Optronic Laboratories with AC lock in detection. Numerical simulations were performed using the Rsoft DiffractMod software package (Rsoft Design Group, Inc., Ossining, NY, USA) and standard literature values for optical constants.[14] Incident light was assumed to be in the form of a plane wave normally incident on the device surface. A simulated absorption spectrum $A(\lambda)$ was computed assuming optical absorption proportional to the square of the electric field amplitude, and the simulated external quantum efficiency was computed assuming 100% efficiency in photogenerated carrier collection.[15] The simulated short-circuit current density, $J_{sc,th}$, computed for AM1.5G incident illumination, is given by

$$J_{sc,th} = e\int A(\lambda)I_{AM1.5}(\lambda)d\lambda, \quad (1)$$

where e is the electron charge magnitude, and $I_{AM1.5}(\lambda)$ is the AM1.5G photon flux density. Quantum well absorption was calculated following the approach given in Ref. 17, with quantum confinement effects, heavy hole-light hole valence band mixing, and excitonic absorption included explicitly in the model. For the nanostructured rear contacts, an array period of 500 nm and modulation depth of 80 nm were chosen considering both device performance and fabrication using the nanosphere lithography process.[16,17]

III. RESULTS AND DISCUSSION

Figure 4(a) shows current-voltage characteristics measured under AM1.5G illumination from a solar simulator for the device structures shown schematically in Figure 3. The measured short-circuit current density, J_{sc}, increases significantly from the GaAs homojunction reference device (8.68 mA/cm^2) to the GaAs/$In_{0.30}Ga_{0.70}As$ quantum-well solar cell with a planar rear contact (9.52 mA/cm^2) to the quantum-well solar cell with a nanostructured rear contact (10.18 mA/cm^2). These increases are associated with

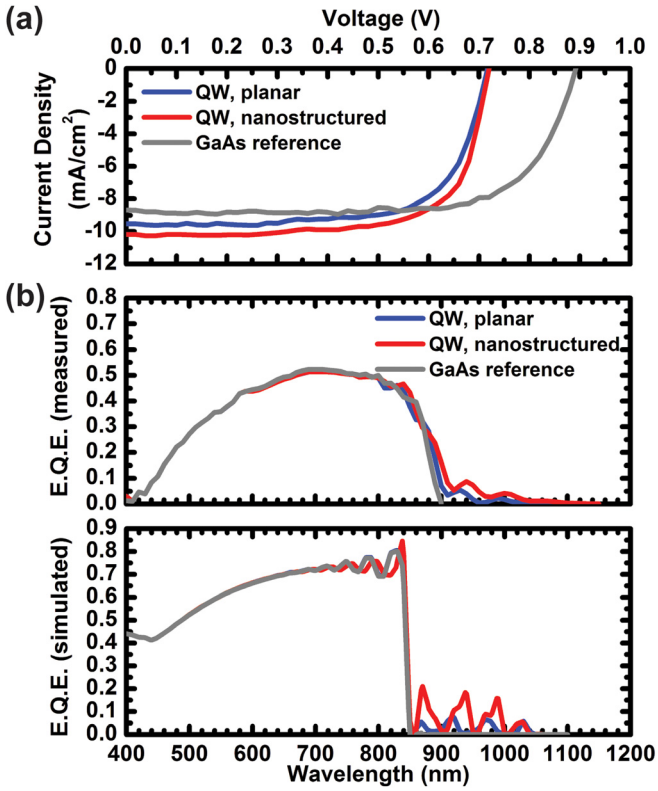

FIG. 4. (a) Current density-voltage characteristics measured under AM1.5G 1-sun illumination from a solar simulator for a GaAs pn homojunction reference device, and for GaAs/$In_{0.30}Ga_{0.70}As$ quantum-well solar cell devices with either planar or nanostructured rear contacts for light trapping. (b) Measured and simulated EQE for all three device types.

absorption in the $In_{0.30}Ga_{0.70}As$ quantum wells that does not occur in the GaAs reference device, and that is enhanced via (i) Fabry-Perot resonances in the quantum-well device with a planar rear contact, and (ii) both Fabry-Perot resonances and coupling to thin-film guided modes that occur with a nanostructured rear contact. A reduction in open-circuit voltage is observed for the quantum-well solar cell devices, which we attribute to a combination of the large conduction-band offset of the $In_{0.30}Ga_{0.70}As$ quantum wells and the possibility of partial strain relaxation; this reduction is undesirable, but incidental to the demonstration and analysis of light trapping effects presented here.

Figures 4(b) and 4(c) show external quantum efficiency (EQE) measured experimentally and simulated numerically for the same set of device structures. In the measured spectra, EQE for all devices at wavelengths shorter than the GaAs absorption edge at ~900 nm are very similar, and limited by reflection from the semiconductor surface (for simplicity antireflection coatings were not included), and by carrier recombination at the top GaAs surface. At wavelengths longer than ~900 nm, optical absorption occurs only in the $In_{0.30}Ga_{0.70}As$ quantum wells. Peaks in the photocurrent response spectra for quantum-well solar cell devices with both planar and nanostructured rear contacts are observed, and as described below are associated with Fabry-Perot resonances (in both device structures) and scattering of light into guided modes within the semiconductor layer (with the nanostructured rear contact). We also note that the measured EQE in the device with a nanostructured rear contact reaches a value as high as 0.087—approximately three times higher than the ~0.01 per quantum well level typically achieved in quantum well solar cells.[18] Furthermore, EQE of 1% per quantum well is maintained via light trapping effects for wavelengths as long as 1060 nm, substantially longer than in prior studies with shallower quantum wells.[18]

Several features are evident in the simulated spectra shown in Figure 4(c). At wavelengths shorter than the GaAs band gap at ~850 nm, the simulated EQE for all devices is limited by surface reflectance; surface carrier recombination is neglected in these simulations, and the difference between

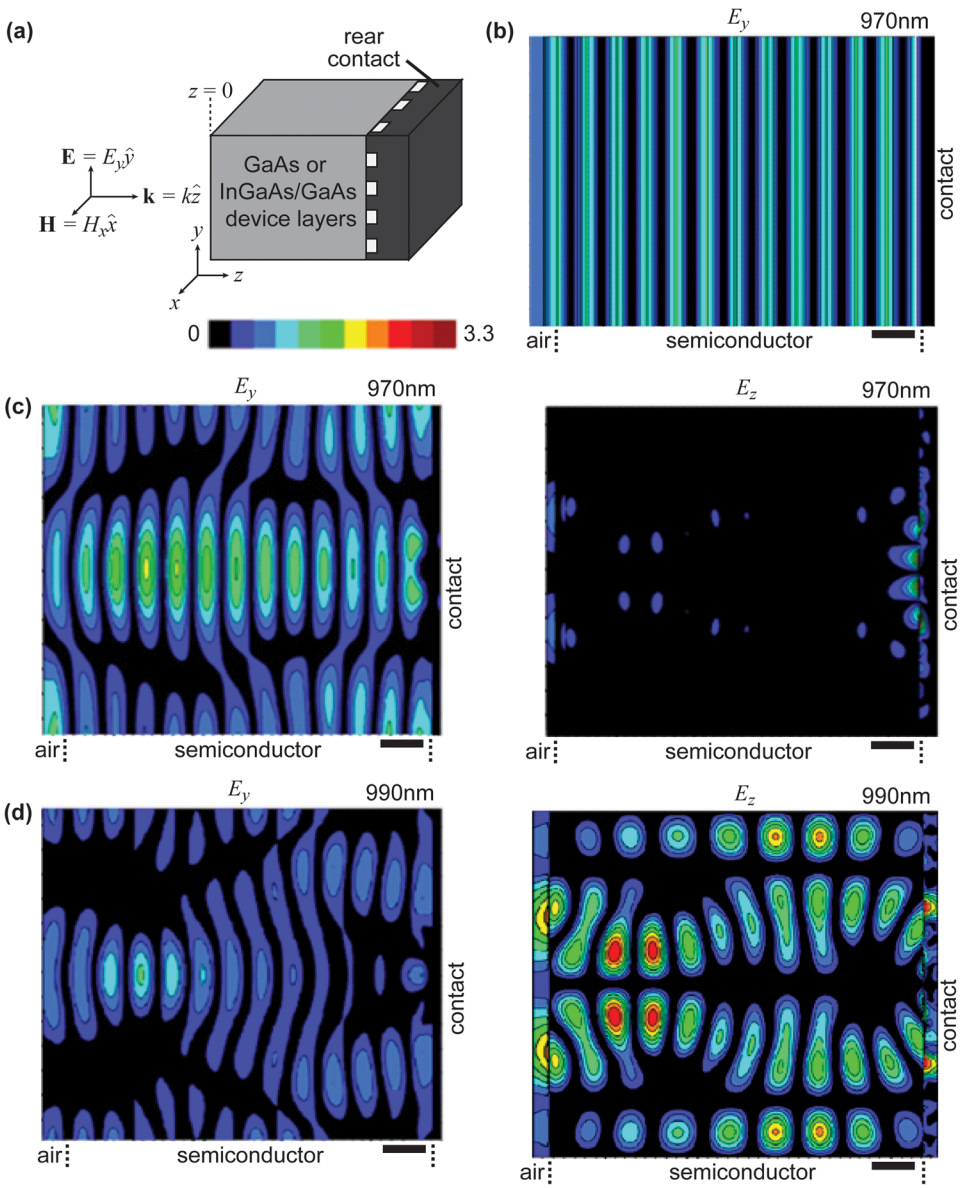

FIG. 5. (a) Schematic diagram of incident field and device geometry for simulations. (b)-(d) Plots of simulated electric field distributions for light incident on quantum-well solar cells with either planar or nanostructured rear contacts at 970 nm or 990 nm, with the incident electric field polarized along the y direction. (b) E_y at 970 nm for cell with planar metal rear contact; E_z is negligible in this situation. (c) E_y and E_z at 970 nm for cell with nanostructured rear contact; (d) E_y and E_z at 990 nm for cell with nanostructured rear contact. Scale bar for all field plots is 200 nm.

the measured and simulated spectra at wavelengths <850 nm is due primarily to surface recombination in the measurements. Numerical estimates based on a standard drift-diffusion analysis accounting for nonradiative surface recombination indicate that the difference between the simulated and measured spectra in this wavelength range can be accounted for by a GaAs surface recombination velocity of $\sim 10^6$ cm/s, a reasonable value given the dopant concentration of $2.5 \times 10^{18}\,\mathrm{cm}^{-3}$ at the device surface.[19] At wavelengths of ~700–850 nm, oscillations in the simulated EQE with wavelength are observed; these arise from Fabry-Perot resonances within the solar cell that occur because GaAs is weakly absorbing at wavelengths near its band gap and multiple passes are required for complete absorption. With a nanostructured rear contact, the resonances are shifted to slightly longer wavelengths due to the presence of dielectric material (SiO_2) within the rear contact structure that increases the effective thickness of the device.[16] At longer wavelengths, for which optical absorption occurs only in the quantum wells, several peaks are observed. With a planar rear contact, these are associated with Fabry-Perot resonances that enable increased absorption in the quantum wells. Similar behavior has been observed previously in quantum-well solar cells grown atop distributed Bragg reflector multilayers.[20] With a nanostructured rear contact, the observed peaks and shoulders are associated with either Fabry-Perot resonances or scattering of light into guided optical modes within the device. Because of the existence of strong Fabry-Perot and guided mode coupling effects, excitonic peaks in the photocurrent response spectral are greatly obscured in this situation.

Simulations provide insight into the origin of photocurrent response enhancement at different wavelengths and for illumination at different angles of incidence. Figure 5 shows simulated electric fields for light incident on quantum-well solar cells with either planar or nanostructured rear contacts at 970 nm or 990 nm, with the incident electric field polarized along the *y* direction. At 970 nm, the electric fields in the semiconductor are predominantly along the *y* direction for devices with both types of rear contacts, indicating that in both cases the enhancement in simulated EQE at 970 nm is associated with a Fabry-Perot resonance. With nanostructured contacts, the variation along the *y* direction in E_y and the nonzero amplitude for E_z at 970 nm, shown in Figure 5(c), arise from scattering by the nanostructured rear contact. A similar analysis has confirmed that the simulated EQE peaks at 870 nm, 920 nm, and 1030 nm for devices with both planar and nanostructured rear contacts arise from Fabry-Perot resonances. At 990 nm, Figure 5(d) shows that the electric field in the semiconductor with a nanostructured rear contact is primarily in the *z* direction, indicating that at this wavelength the incident light is strongly scattered into a guided optical mode and propagates in a direction orthogonal to that of the incident light. A similar analysis has confirmed that the simulated EQE peaks at 890 nm and 940 nm for the device with a nanostructured rear contact arises from similar scattering behavior. For the quantum-well solar cell with a planar rear contact, peaks are observed in measured EQE at 930 nm, 990 nm, and 1050 nm, corresponding to the simulated peaks at 920 nm, 970 nm, and 1030 nm; differences between the simulated and measured peak positions are attributed to small differences between the simulated and experimentally fabricated structures. With a nanostructured rear contact, the measured EQE contains peaks at 930 nm, 980 nm, and 1040 nm, corresponding to combinations of closely spaced Fabry-Perot and scattering peaks at 920–940 nm, 970–990 nm, and 1030–1050 nm in the simulated spectrum. The measured peaks are generally lower in amplitude, but broader, than the simulated peaks, with the integrated contributions to total photocurrent density being very similar between simulation and experiment.

Comparison of the increases in $J_{sc,th}$ upon introduction of the $In_{0.30}Ga_{0.70}As$ quantum wells and then the nanostructured rear contacts with experimentally measured values demonstrates very good agreement between simulation and experiment. $J_{sc,th}$ for the quantum-well solar cell with a planar rear contact is 0.90 mA/cm^2 higher than for the GaAs reference homojunction device, in very good agreement with the measured increase in J_{sc} of 0.84 mA/cm^2. Introduction of the nanostructured rear contact leads to a further increase in $J_{sc,th}$ of 0.70 mA/cm^2, again in very good agreement with the measured value of 0.66 mA/cm^2. The combination of $In_{0.30}Ga_{0.70}As$ quantum wells and nanostructured rear contacts yields a measured increase in J_{sc} of 1.50 mA/cm^2, or ~17%, compared to the GaAs reference solar cell, in very good agreement with an increase of 1.60 mA/cm^2 predicted

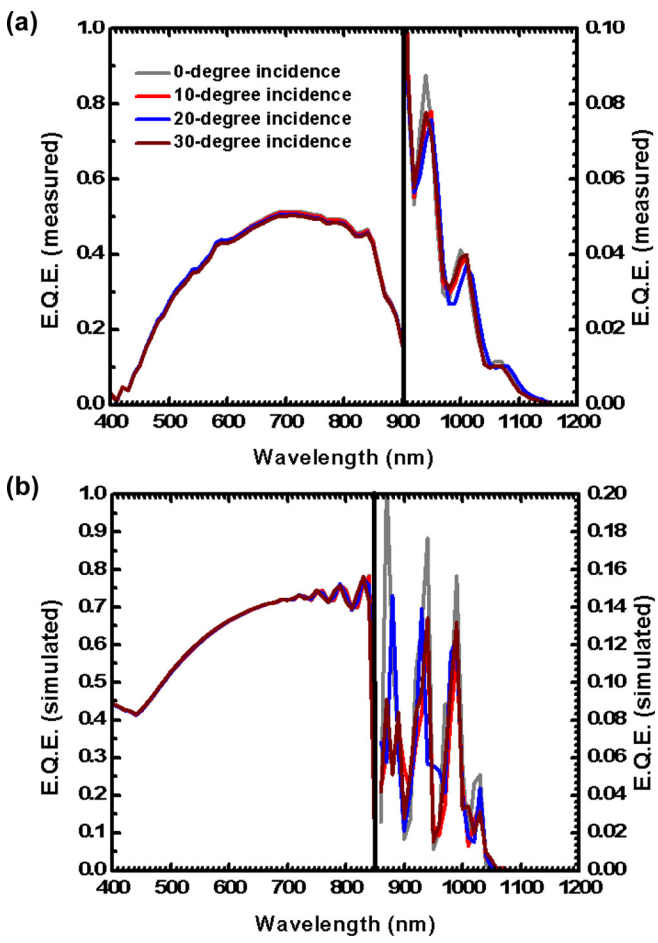

FIG. 6. (a) Measured and (b) simulated EQE spectra of quantum-well solar cell with nanostructured back contact under different incident angles.

via simulations. These results confirm that such simulations provide good guidance with regard to experimentally realizable improvements achievable by these approaches, and earlier simulation studies[17] have suggested that substantially larger increases can be achieved via optimization of quantum well composition and structure and of the period and composition of nanostructured rear contacts.

To further investigate the nature of the light trapping mechanism for the devices with nanostructured rear contacts, we simulated and measured EQE spectra as a function of incident angle. Figure 6(a) shows measured EQE spectra for angles of incidence from normal incidence up to 30-degree off normal incidence, Over this range of incident angles, three broad peaks are observed in the measured photocurrent response at wavelengths >900 nm, for which absorption occurs primarily in the InGaAs quantum wells. Figure 6(b) shows simulated EQE spectra for the same angles of incidence. The peaks in simulated photo-current response in the sub-GaAs bandgap region can be seen to shift slightly in wavelength with increasing angle of incidence. The shifts in wavelengths of these peaks with incident angle can be explained by mode dispersion relations based on the Bragg coupling equations as described in more detail below.[21,22]

Figure 7 shows the simulated electric fields for light incident at an angle of 10° off normal on the quantum-well solar cell with nanostructured back contact at wavelengths of 960 nm or 990 nm with incident light polarized along the *y* direction. At 960 nm, Figures 7(a) and 7(b) show that the electric field in the semiconductor with the nanostructured rear contact is primarily along the *z*-direction, indicating that at this wavelength light is strongly guided into an optical mode and propagates in a direction orthogonal to that of the

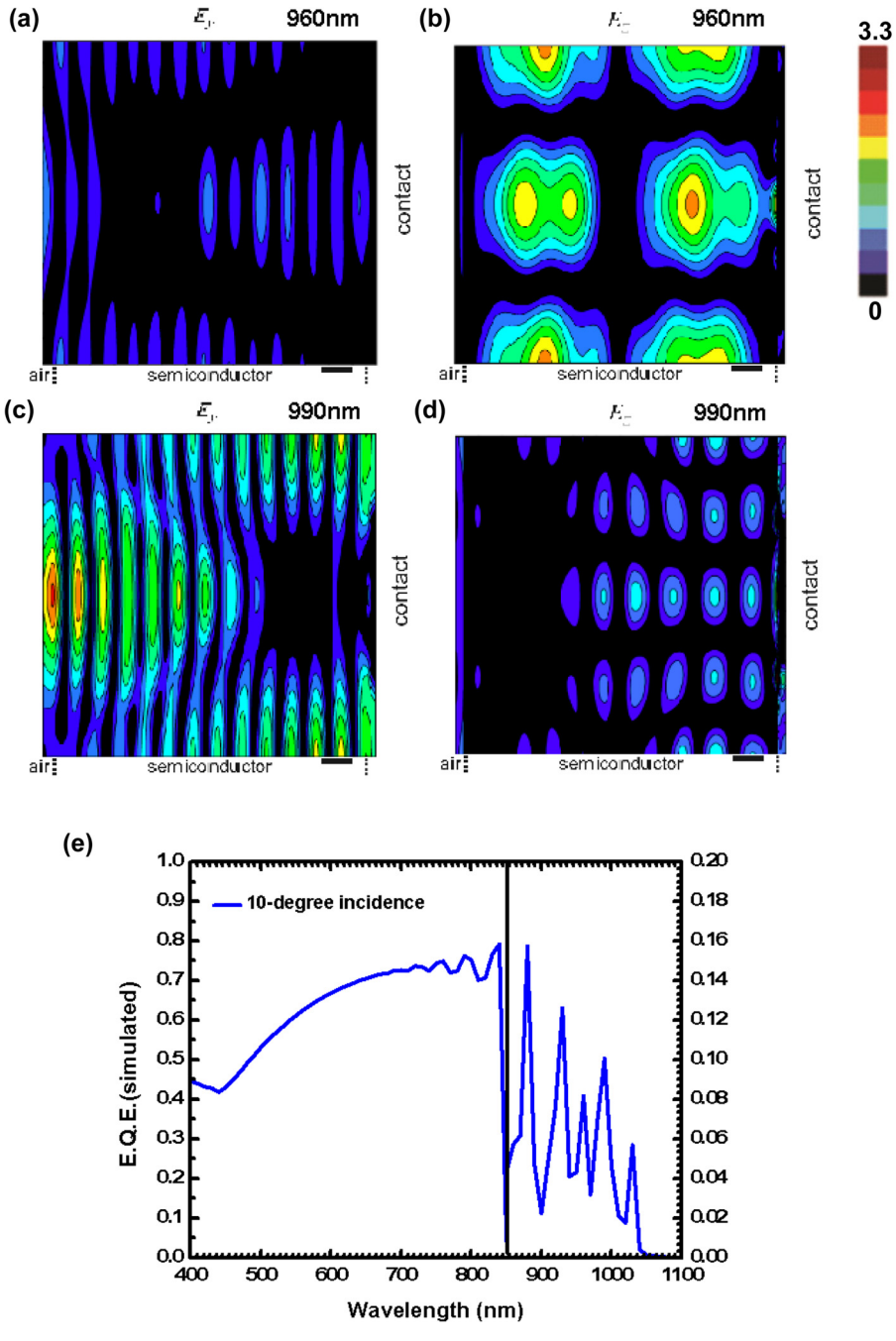

FIG. 7. (a)-(d) Representative plots of simulated electric field distributions for light incident on quantum-well solar cell with nanostructured back contact at an angle of 10° off-normal incidence and at wavelengths of 960 nm or 990 nm, with the incident electric field polarized along the *y* direction. (a) E_y at 960 nm; (b) E_z at 960 nm; (c) E_y at 990 nm; (d) E_z at 990 nm. (e) Simulated EQE spectrum under 10° off-normal incidence of the quantum-well solar cell.

incident light; the corresponding peak in the simulated EQE spectrum shown in Figure 7(e) is therefore interpreted as arising from waveguide mode coupling effect. At 990 nm, Figures 7(c) and 7(d) show that the electric field in the semiconductor is predominantly along the y direction, indicating that the enhancement in the simulated EQE spectrum at this wavelength is associated with Fabry-Perot resonance. The variation along the y direction in E_y and the non-zero amplitude in E_z arise from scattering by the nanostructured back contact. A similar analysis applied to the simulated electric field distributions and EQE spectra under different incident angles enables the dependence of coupling to guided modes and to Fabry-Perot resonances in the device structure on wavelength and angle of incidence to be determined. These dependences are summarized in Figure 8.

To complement the simulations of field distributions and analyze more explicitly the relative roles of guided modes and Fabry-Perot modes for off-normal incidence, we have also calculated the dispersion curves for the guided modes in our device with the nanostructured rear contacts using the Bragg coupling equations.[21] In Figure 8(a), branches corresponding to modes coupling to incident light polarized along the y direction are shown, folded back to the angular range of interest by taking diffraction by the two-dimensional periodic scattering structure into account. In a similar way, we also calculated dispersion curves for Fabry-Perot modes with the same incident polarization, as shown in Figure 8(b). Comparing these calculated dispersion curves with the peak wavelengths in simulated photo-current response, we see that the positions of sub-GaAs bandgap EQE peaks agree well with the calculated mode dispersion. The simulated and measured photoresponse for wavelengths shorter than the GaAs band edge changes relatively little with increasing angle of incidence because the increase in surface reflectivity of s-polarized light with increasing incident angle is partially cancelled by the decreased surface reflectivity of p-polarized light as Brewster's angle is approached.[16] For wavelengths longer than the GaAs bandgap, we observe that the coupling of incident light into optically guided modes does not degrade significantly with the increasing incidence angle, due to the larger number of allowed waveguide modes at off-normal incidence angle as deduced from Bragg coupling condition.[22] The robustness of the observed light trapping effects to variations in angle of incidence is of particular significance for applications both in concentrating photovoltaics, for which concentrated sunlight is typically incident on high-efficiency solar cells over a range of angles, and in non-tracking solar systems in which the angle at which sunlight is incident can vary substantially.

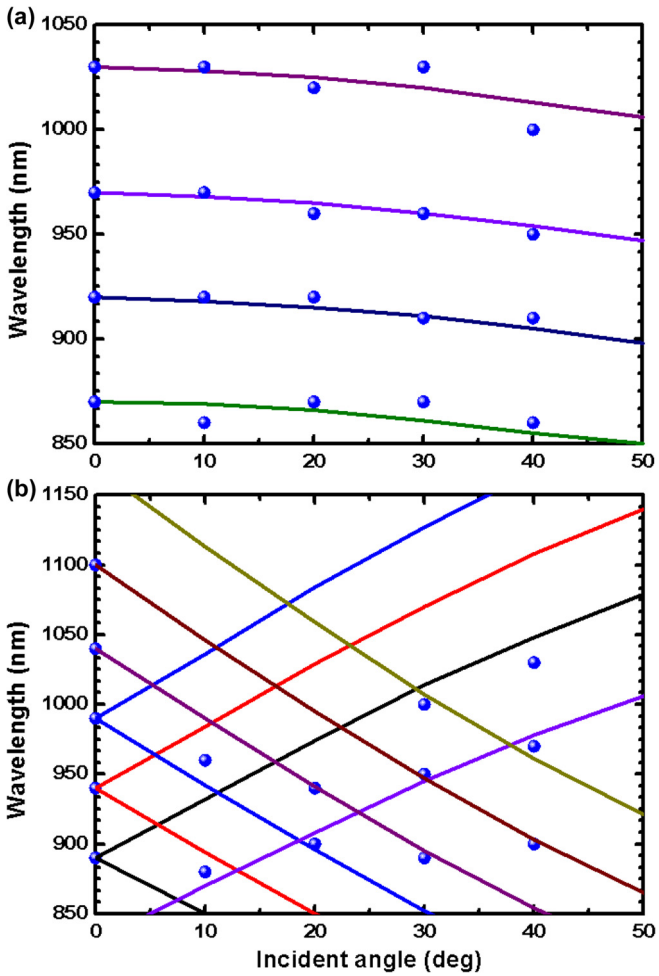

FIG. 8. Dispersion relations for (a) guided modes and (b) Fabry-Perot modes. Symbols correspond to distinguishable peaks in the simulated EQE spectrum with incident light polarized along the y direction.

IV. SUMMARY

In summary, we have designed, fabricated, and characterized GaAs/$In_{0.30}Ga_{0.70}As$ quantum-well solar cells integrated with nanostructured light trapping elements via substrate removal and nanosphere lithography patterning processes. Large increases in photocurrent response and high optical absorption efficiency per quantum well can be achieved and maintained to wavelengths well beyond 1000 nm, with very good agreement between measured and simulated increases in short-circuit current density. Detailed analysis of electric field distributions for light incident at different wavelengths provides insight into the relative contributions to increased photocurrent response of Fabry-Perot resonances and of scattering into guided optical modes both at normal incidence and off-normal incidence, clearly revealing the nature of these effects in providing significant increases in photocurrent response and short-circuit current density.

ACKNOWLEDGMENTS

X.H.L. gratefully acknowledges helpful discussions with Dr. Katsuaki Tanabe for the substrate removal process and part of the device testing work. Part of this work was supported by NSF (Nos. ECCS-1128682 and ECCS-1120823) and the Judson S. Swearingen Regents Chair in Engineering at the University of Texas at Austin.

[1]M. A. Green and S. Pillai, Nat. Photonics **6**, 130–132 (2012).
[2]P. Campbell and M. A. Green, J. Appl. Phys. **62**, 243 (1987).
[3]H. A. Atwater and A. Polman, Nat. Mater. **9**, 205 (2010).
[4]Z. Yu, A. Raman, and S. Fan, Proc. Natl. Acad. Sci. U.S.A. **107**, 17491 (2010).

[5]E. T. Yu and J. van de Lagemaat, MRS Bull. **36**, 424 (2011).
[6]K. W. J. Barnham, I. Ballard, J. P. Connolly, N. J. Ekins-Daukes, B. G. Kluftinger, J. Nelson, and C. Rohr, Physica E (Amsterdam) **14**, 27 (2002).
[7]M. Konagai, M. Sugimoto, and K. Takahashi, J. Cryst. Growth **45**, 277 (1978).
[8]Y. Itoh, T. Nishioka, A. Yamamoto, and M. Yamaguchi, Appl. Phys. Lett. **49**, 1614 (1986).
[9]N. J. Ekins-Daukes, K. W. J. Barnham, J. P. Connolly, J. S. Roberts, J. C. Clark, G. Hill, and M. Mazzer, Appl. Phys. Lett. **75**, 4195 (1999).
[10]K. W. J. Barnham and G. Duggan, J. Appl. Phys. **67**, 3490 (1990).
[11]K. Tanabe, K. Watanabe, and Y. Arakawa, Appl. Phys. Lett. **100**, 192102 (2012).
[12]C. L. Haynes, A. D. McFarland, M. T. Smith, J. C. Hulteen, and R. P. Van Duyne, J. Phys. Chem. **106**, 1898 (2002).
[13]J. Rybczynski, U. Ebels, and M. Giersig, Colloids Surf. **219**, 1 (2003).
[14]E. D. Palik, *Handbook of Optical Constants of Solids* (Academic Press, New York, 1998).
[15]S. R. Forrest, MRS Bull. **30**, 28 (2005).
[16]X. H. Li, P. C. Li, D. Hu, D. M. Schaadt, and E. T. Yu, Appl. Phys. Lett. **114**, 044310 (2013).
[17]C. O. McPheeters and E. T. Yu, Opt. Express **20**, A864 (2012).
[18]D. B. Bushnell, T. N. D. Tibbits, K. W. J. Barnham, J. P. Connolly, M. Mazzer, N. J. Ekins-Daukes, J. S. Roberts, G. Hill, and R. Airey, J. Appl. Phys. **97**, 124908 (2005).
[19]S. M. Sze, *Physics of Semiconductor Devices* (John Wiley & Sons, New York, 1981), pp. 800–805.
[20]D. B. Bushnell, N. J. Ekins-Daukes, K. W. J. Barnham, J. P. Connolly, J. S. Roberts, G. Hill, R. Airey, and M. Mazzer, Sol. Energy Mater. Sol. Cells **75**, 299 (2003).
[21]P. Spinelli, V. E. Ferry, J. van de Groep, M. van Lare, M. A. Verschuuren, R. E. I. Schropp, H. A. Atwater, and A. Polman, J. Opt. **14**, 024002 (2012).
[22]V. E. Ferry, M. A. Verschuuren, H. B. T. Li, R. J. Walters, R. E. I. Schropp, H. A. Atwater, and A. Polman, Opt. Express **18**, A237 (2010).
[23]Y. C. Chen and P. K. Bhattacharya, J. Appl. Phys. **73**, 7389 (1993).